



Cite this: *Phys. Chem. Chem. Phys.*,  
2016, **18**, 16423

# Methane adsorption and dissociation on iron oxide oxygen carriers: the role of oxygen vacancies

Zhuo Cheng,<sup>a</sup> Lang Qin,<sup>a</sup> Mengqing Guo,<sup>a</sup> Jonathan A. Fan,<sup>b</sup> Dikai Xu<sup>a</sup> and Liang-Shih Fan<sup>\*a</sup>

We performed *ab initio* DFT+*U* calculations to explore the interaction between methane and iron oxide oxygen carriers for chemical looping reaction systems. The adsorption of CH<sub>4</sub> and CH<sub>x</sub> (*x* = 0–3) radicals on  $\alpha$ -Fe<sub>2</sub>O<sub>3</sub>(001), and the influence of oxygen vacancies at the top surface and on the subsurface on the adsorption properties of the radicals was investigated. The adsorption strength for CH<sub>4</sub> and C radicals at the top of the  $\alpha$ -Fe<sub>2</sub>O<sub>3</sub>(001) surface in the presence of oxygen vacancies is lower than that on the stoichiometric surface. However, for methyl (CH<sub>3</sub>), methylene (CH<sub>2</sub>) and methine (CH) radicals, it is correspondingly higher. In contrast, the oxygen vacancy formation on the subsurface not only increases the adsorption strength of CH<sub>3</sub>, CH<sub>2</sub> and CH radicals, but also facilitates C radical adsorption. We found that oxygen vacancies significantly affect the adsorption configuration of CH<sub>x</sub> radicals, and determine the probability of finding an adsorbed species in the stoichiometric region and the defective region at the surface. With the obtained adsorption geometries and energetics of these species adsorbed on the surface, we extend the analysis to CH<sub>4</sub> dissociation under chemical looping reforming conditions. The distribution of adsorbed CH<sub>4</sub> and CH<sub>x</sub> (*x* = 0–3) radicals is calculated and analyzed which reveals the relationship between adsorbed CH<sub>x</sub> radical configuration and oxygen vacancies in iron oxide. Also, the oxygen vacancies can significantly facilitate CH<sub>4</sub> activation by lowering the dissociation barriers of CH<sub>3</sub>, CH<sub>2</sub> and CH radicals. However, when the oxygen vacancy concentration reaches 2.67%, increasing the oxygen vacancy concentration cannot continue to lower the CH dissociation barrier. The study provides fundamental insights into the mechanism of CH<sub>4</sub> dissociation on iron based oxygen carriers and also provide guidance to design more efficient oxygen carriers.

Received 25th February 2016,  
Accepted 20th May 2016

DOI: 10.1039/c6cp01287f

www.rsc.org/pccp

## 1 Introduction

Chemical looping combustion (CLC) is a novel combustion technique in which metal oxide oxygen carriers are used as the oxygen source for heat generation.<sup>1,2</sup> The CLC operation uses two reactors that are interconnected. One is a fuel reactor in which metal oxides are reduced by reacting them with the carbonaceous feedstock and the other one is an air reactor in which the reduced metal oxides from the fuel reactor are regenerated by re-oxidization with air. In the fuel reactor, CO<sub>2</sub> generated from the oxidation reaction can be captured with 100% efficiency from the outlet of the reactor by simply condensing the steam, another reaction product, without engaging complex CO<sub>2</sub> separation schemes. When biomass is used as

the fuel, carbon emission in the life cycle assessment from chemical looping processes can be negative.<sup>3</sup> This technology has been developed into a chemical looping partial oxidation (CLPO) process for direct syngas production from methane with significant economic attraction compared to the conventional approaches. In the CLPO process, oxygen carriers provide oxygen to partially oxidize methane in the fuel reactor or the reducer, thereby undergoing reduction themselves. The reduced oxygen carriers are then regenerated by air in the air reactor or the combustor and circulated back to the reducer. The oxidation reactions occurring in the combustor are highly exothermic and the heat generated can be used for power generation. The CLPO process can generate separate streams of high purity syngas from the reducer and an O<sub>2</sub>-depleted flue gas from the combustor, which obviates many downstream processing steps for the product generation, as illustrated in Fig. 1. This technique has been transformative and yields a highly efficient process of high economic benefits in the conversion of methane to syngas and hence a vast array of high value chemicals.<sup>4,5</sup>

<sup>a</sup> Department of Chemical and Biomolecular Engineering, The Ohio State University, 140 West 19th Ave, Columbus, OH 43210, USA. E-mail: fan.1@osu.edu

<sup>b</sup> Department of Electrical Engineering, Ginzton Laboratory, Spilker Engineering and Applied Sciences, Stanford University, 348 Via Pueblo Mall, Stanford, CA 94305, USA

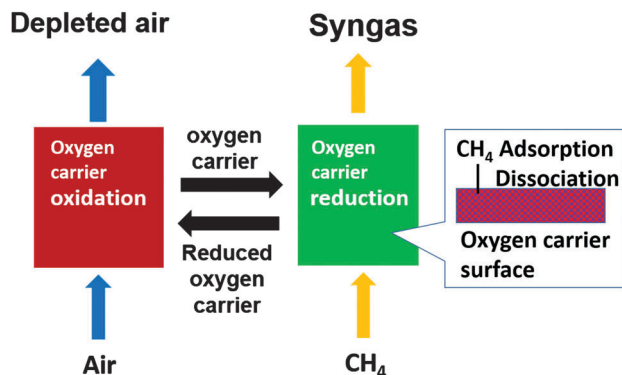


Fig. 1 The basic principles of  $\text{CH}_4$  chemical looping reformation.  $\text{CH}_4$  and  $\text{CH}_x$  radical adsorption and dissociation occur in the reduction section of the chemical looping system.

Oxygen carriers play an important role in determining the product quality and process efficiency for the CLPO process. During reduction, the oxygen carrier donates the required amount of lattice oxygen for methane partial oxidation and form oxygen vacancies. In the oxidation step, the depleted oxygen carriers are replenished with oxygen from air while the oxygen vacancies are healed. Extensive research has been conducted in the design and development of efficient oxygen carriers. Oxygen carriers for successful chemical looping operation need to possess certain properties like high oxygen-carrying capacity, high fuel conversion, good redox reactivity, fast kinetics, good recyclability, long-term stability, high attrition resistance, good heat-carrying capacity, high melting point, resistance to toxicity, and low production cost. In addition, the applications for partial oxidation require certain distinct oxygen carrier properties to accurately control the product selectivity. Various oxygen carriers have been studied for CLPO applications, such as transition metal oxides of Co, Ni, Cu, Mn, W and Fe.<sup>6–11</sup> Among these oxygen carriers, iron oxide is very attractive since it is relatively inexpensive, readily available from large natural reserves and also environmentally safe.<sup>12–14</sup>

Some studies of methane partial oxidation on iron oxide have been performed in recent years. Luo *et al.*<sup>15</sup> demonstrated that the  $\text{Fe}_2\text{O}_3$ -based oxygen carrier can generate syngas at a concentration higher than 90%, balanced by  $\text{CO}_2$  and steam, with full fuel conversion. In their unique moving bed reactor configuration, the reactor is designed to operate with minimal carbon deposition and without the use of steam. The feedstock can be methane, biomass, coal, and other types of carbonaceous fuels, and  $\text{H}_2/\text{CO}$  may vary from 1:1 to 3:1 depending on the feedstock and operating conditions. Monazam *et al.*<sup>16</sup> used thermogravimetric analysis to investigate the reduction of  $\text{Fe}_2\text{O}_3$  in the methane atmosphere over the range of 700–825 °C with a continuous stream of  $\text{CH}_4$  (15%, 20%, and 35%), and found that most of the  $\text{CH}_4$  was totally oxidized into  $\text{CO}_2$  and  $\text{H}_2\text{O}$  at the early stages of the reduction period, then  $\text{CO}$  and  $\text{H}_2$  were released due to partial oxidation of  $\text{CH}_4$ . Jin *et al.*<sup>17</sup> studied the reduction of  $\text{Fe}_2\text{O}_3$  and evolution of gas products during  $\text{CH}_4$  oxidation using TGA-MS under different reaction atmospheres, and reported that the ventilation air will hamper  $\text{CH}_4$  oxidation.

As the key step of  $\text{CH}_4$  oxidation, the C–H bond dissociation on metal surfaces has been intensively studied. Killelea *et al.* used state-resolved gas-surface scattering measurements which showed that the C–H stretch vibration selectively activates C–H bond cleavage on a Ni(111) surface.<sup>18</sup> Smith *et al.* reported that vibrational excitation of the antisymmetric C–H stretching activates methane dissociation more efficiently than translational energy.<sup>19</sup> Yoder *et al.* presented a stereodynamics study of the chemisorption of vibrationally excited methane on the (100) surface of nickel, and found that the alignment of the vibrational transition dipole moment of methane is responsible for the steric effect.<sup>20</sup> Krishnamohan *et al.* used quantum dynamics calculations to investigate the  $\text{CH}_4$  reactivity on Ni(111) and concluded that the bending vibration greatly affects dissociation.<sup>21</sup> Nave and Jackson<sup>22</sup> found that the Ni lattice reconstructs can effectively lower the C–H dissociation barrier based on first principles calculations, and also Tiwari *et al.*<sup>23</sup> found that the thermal vibrations of the Ni lattice strongly modify the  $\text{CH}_4$  reactivity. However, the interaction between iron oxides and methane has not still been fully understood due to the complex nature of  $\text{Fe}_2\text{O}_3$  and limitations in experimentally detecting the dissociated  $\text{CH}_x$  radicals on the reaction surface using current spectroscopic techniques.

In addition, the relationships between oxygen carrier activity and its defective structure, especially oxygen vacancies, are not clear. As mentioned above, the oxygen carrier will donate lattice oxygen during methane partial oxidation which leads to the formation of oxygen vacancies. The vacancy sites act as initiators for the adsorption of molecules in many surface reactions.<sup>24–28</sup> It is therefore important to discern the stability of the different oxygen vacancies on the iron oxide surface, and their effect on the interaction between methane and oxygen carriers.

*Ab initio* DFT+U calculations can complement experimental mechanistic studies and provide valuable information on the structure of the active sites and the energy of the adsorbed species interacting with the surfaces.<sup>29–31</sup> In addition, detailed reaction pathways can be derived and characterized by the energy profile of the constituent elementary steps.<sup>32</sup> There have been a few DFT studies on the defect properties of  $\text{Fe}_2\text{O}_3$ . Warschkow *et al.*<sup>33</sup> built a slab model of the (001) surface of hematite as well as the bulk structure, and found that point defects are easier to form if they are closer to the top layer of surfaces, which is in agreement with our previous reported results.<sup>34</sup> Wanaguru *et al.*<sup>35</sup> modeled hematite nanoribbons, and showed that built-in oxygen vacancies can be produced on the edge. However, these studies only focus on the solid state and have not considered the relative surface reaction. Although the  $\text{CH}_4$  dissociation mechanism for various materials has been widely studied,<sup>36–39</sup> there are few reports on the  $\text{CH}_4$  dissociation mechanism on iron oxide. Wang *et al.*<sup>40</sup> have used the density functional theory (DFT) method to investigate the interaction between  $\text{CH}_4$  and  $\text{Fe}_2\text{O}_3$  but they only used a  $\text{Fe}_2\text{O}_3$  cluster model and did not include the oxygen vacancies in their system. No work has been reported on the effect of  $\text{Fe}_2\text{O}_3$  vacancies on  $\text{CH}_4$  and  $\text{CH}_x$  radical adsorption and the corresponding  $\text{CH}_4$  dissociation mechanism as far as we know. The lack of this knowledge will

hamper the design and development of oxygen carriers. Therefore, a detailed study of the role of oxygen vacancies in CH<sub>4</sub> adsorption and dissociation at the atomic level is highly desirable.

In this study, we present DFT+*U* and thermochemistry analysis of CH<sub>4</sub> and CH<sub>*x*</sub> (*x* = 0–3) radical adsorption and dissociation on the stoichiometric α-Fe<sub>2</sub>O<sub>3</sub>(001) surface and the defective α-Fe<sub>2</sub>O<sub>3</sub>(001) surface with different oxygen vacancies. The study of adsorption and dissociation with vacancy defects will directly be of value to the future computational quantum mechanical and thermodynamic account of the partial oxidation pathways and to design more efficient oxygen carriers for the CLPO process.

## 2 Computational model and method

The first-principles calculations were performed within the framework of density functional theory (DFT), using the Vienna Ab Initio Simulation Package (VASP).<sup>41–43</sup> The generalized gradient approximation of Perdew, Burke and Ernzerhof<sup>44</sup> was used to represent the exchange–correlation energy. The projector-augmented wave (PAW) method,<sup>45,46</sup> with a 400 eV energy cutoff, was used to describe the wave functions of the atomic cores. The tetrahedron method with Blöchl corrections<sup>47</sup> was used to set the partial occupancies for the orbitals. The calculated α-Fe<sub>2</sub>O<sub>3</sub> bulk lattice parameters were *a* = *b* = 5.04 Å and *c* = 13.83 Å, in good agreement with the experimental values (*a* = *b* = 5.038 Å and *c* = 13.772 Å).<sup>48</sup> The α-Fe<sub>2</sub>O<sub>3</sub>(001) surface with Fe–O<sub>3</sub>–Fe-termination was chosen to model the iron oxide slab with a thickness of ~15 Å. We used (2 × 2) surface unit cells, and a vacuum region of 20 Å which ensures negligible interaction between periodic replicas. While several *k*-point mesh sizes (e.g., 4 × 4 × 1 up to 13 × 13 × 1) were considered, ultimately the 8 × 8 × 1 Monkhorst–Pack *k*-point mesh was used for surface calculations. Geometries were optimized until the energy had converged to 1.0 × 10<sup>−5</sup> eV per atom and the force converged to 0.01 eV Å<sup>−1</sup>. The spin restricted method was used for the investigation of the oxygen vacancy formation on the α-Fe<sub>2</sub>O<sub>3</sub>(001) surface and spin-unrestricted calculations for the study of the CH<sub>*x*</sub> radical (*x* = 0–3) adsorption on the stoichiometric and reduced α-Fe<sub>2</sub>O<sub>3</sub>(001), respectively. The on-site Coulomb repulsion amongst the localized 3d electrons is not described very well in a spin-polarized DFT treatment. To consider this Coulomb repulsion explicitly, we used DFT+*U* correction, which consists of combining DFT with a Hubbard–Hamiltonian term.<sup>49,50</sup> Increasing *U* from 1 eV to 4 eV results in improved values for magnetic moments and band gaps as well as better agreement with density of states by experimental IPS spectra. A further increase in *U* cannot achieve better agreement. In addition, the band gap becomes too large and occupied Fe 3d states are shifted to too low energies, i.e., *U* > 4.2 eV. Therefore, we choose *U* = 4 eV to describe the energy required for adding an extra d electron to the Fe atom.<sup>51</sup>

The oxygen vacancy formation energies are calculated based on the following expression:

$$E_f = E_{\text{tot}} = E_V - \frac{1}{2}E_{\text{O}_2} \quad (1)$$

In eqn (1), *E*<sub>tot</sub> is the total energy of the stoichiometric surface, *E*<sub>V</sub> is the total energy of the reduced surface with one oxygen vacancy, and *E*<sub>O<sub>2</sub></sub> is the total energy of the optimized gas phase O<sub>2</sub>. The adsorption energies of CH<sub>*x*</sub> (*x* = 0–3) radicals on the stoichiometric and reduced surfaces are calculated using the expression as follows:

$$E_{\text{ad}} = E_{\text{CH}_x} + E_{\text{surf}} - E_{(\text{CH}_x+\text{surf})} \quad (2)$$

where *E*<sub>CH<sub>*x*</sub></sub> is the energy of the optimized gas phase geometry of CH<sub>*x*</sub>, *E*<sub>surf</sub> is the total energy of the respective surface, and *E*<sub>(CH<sub>*x*</sub>+surf)</sub> is the total energy of the slab with adsorbed CH<sub>*x*</sub>. Based on this definition, a more positive *E*<sub>ad</sub> corresponds to a more stable configuration.

The C atom of CH<sub>*x*</sub> radicals may bond to lattice oxygen atoms on the surface. To analyze the bonding effect and strength, the bond order *n* of the C–O bond has been calculated as follows:

$$n = aR^{-2} - b \quad (3)$$

where *R* is the C–O bond length in Å. According to Gordy theory, we can set *a* = 5.75 Å<sup>2</sup> and *b* = 1.85.<sup>52</sup>

For CH<sub>4</sub> dissociation barrier calculations, the climbing-image nudged elastic band (CI-NEB) method was used.<sup>53,54</sup> This method enabled the stationary points to be mapped out along the minimum energy paths and identify transition states for each of the diffusion processes. Because these paths were directed by force projection, the energy was not necessarily consistent with the force being optimized; thus, the force-based optimizer was chosen to ensure the convergence of the nudged elastic band algorithm.

## 3 Results and discussion

### 3.1 Oxygen vacancy formation

Iron oxide has been proved to be an efficient oxygen carrier for reduction–oxidation (redox) chemistry in CH<sub>4</sub> chemical looping reformation, where it mediates CH<sub>4</sub> oxidation through the release of oxygen. In this process, adsorbed CH<sub>*x*</sub> radicals on the surface accept an oxygen atom from the iron oxide and the oxygen vacancy is created. The calculated formation energies for different surface and subsurface oxygen vacancy defects (*V*<sub>O</sub>) at the α-Fe<sub>2</sub>O<sub>3</sub>(001) surface are reported in Table 1. The labeling of the different vacancy sites is shown in Fig. 2.

By removing a 3-fold bridging oxygen (O3c), the vacancy on the top surface *V*<sub>O</sub>(1) can be created. It results in one 2-fold coordinated Fe (Fe2c) and two 5-fold coordinated Fe (Fe5c). This is found to be the energetically most favorable oxygen vacancy with the vacancy formation energy of 258.56 kJ mol<sup>−1</sup>, while the vacancy formation energies for *V*<sub>O</sub>(2) and *V*<sub>O</sub>(2) are 292.51 kJ mol<sup>−1</sup> and 342.43 kJ mol<sup>−1</sup>, respectively (Table 1). The Fe–O bonds of the neighboring Fe2c become symmetric with a bond length of 2.03 Å when the *V*<sub>O</sub>(1) oxygen vacancy is formed. The fact that the slight atom movement requires less energy and will not cause breaking of the neighboring bond makes *V*<sub>O</sub>(1) the most stable vacancy. The vacancy on the subsurface *V*<sub>O</sub>(2) can be created by removing a 4-fold bridging oxygen (O4c),

**Table 1** Energy of formation for different oxygen vacancies in  $\alpha$ -Fe<sub>2</sub>O<sub>3</sub>(001), the minimal and maximal length of Fe–O bonds around the vacancy ( $d_{\min}$  and  $d_{\max}$ , respectively), and the probability of V<sub>O</sub>(2) and V<sub>O</sub>(3) vacancies at 700 °C and 900 °C (relative to V<sub>O</sub>(1))

	$E_f$ (kJ mol <sup>−1</sup> )	$d_{\min}$ (Å)	$d_{\max}$ (Å)	Relative probability at 700 °C (%)	Relative probability at 900 °C (%)
V <sub>O</sub> (1)	258.56	2.03	2.03	100	100
V <sub>O</sub> (2)	292.51	1.93	2.09	1.51	3.07
V <sub>O</sub> (3)	342.43	1.91	2.13	$3.13 \times 10^{-5}$	$1.84 \times 10^{-4}$

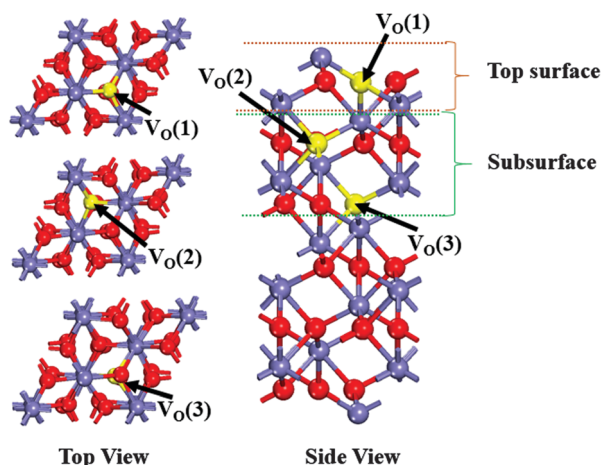


**Fig. 2**  $\alpha$ -Fe<sub>2</sub>O<sub>3</sub>(001) slab model with oxygen vacancies on the top surface and the subsurface (Fe = purple, O = red, oxygen vacancy = yellow).

and this process leads to asymmetric Fe–O bonds ranging from 1.93 Å to 2.09 Å. Similarly, the vacancy on the next subsurface V<sub>O</sub>(3) is also formed by removing a 4-fold bridging oxygen (O4c). However, V<sub>O</sub>(3) formation energy is 83.87 kJ mol<sup>−1</sup> higher than V<sub>O</sub>(1) formation energy. Therefore, for  $\alpha$ -Fe<sub>2</sub>O<sub>3</sub>(001), the oxygen vacancies on the top surface are more stable than the vacancies on the subsurface, which is different from anatase TiO<sub>2</sub> in which the oxygen vacancies on the subsurface are more stable.<sup>55</sup>

The presence probabilities of the different oxygen vacancies of  $\alpha$ -Fe<sub>2</sub>O<sub>3</sub>(001) at 700 °C and 900 °C are also shown in Table 1. It is found that V<sub>O</sub>(3) does not play a significant role in the adsorption of CH<sub>4</sub> and CH<sub>x</sub> radicals ( $x = 0$ –3) due to high formation energy and low probability.

### 3.2 Adsorption of CH<sub>4</sub> and CH<sub>x</sub> radicals on $\alpha$ -Fe<sub>2</sub>O<sub>3</sub>(001)

In this section, we discuss the adsorption of methane and the dissociated radical species on  $\alpha$ -Fe<sub>2</sub>O<sub>3</sub>(001) as well as the influence of the different oxygen vacancies (V<sub>O</sub>(1) on the top surface and V<sub>O</sub>(2) in subsurface) on this adsorption. The different adsorption configurations are indicated as CH<sub>x</sub>@S-y or CH<sub>x</sub>@V<sub>O</sub>(n)-y, where  $x$  (0–4) is the adsorbed species (CH<sub>4</sub>, CH<sub>3</sub>, CH<sub>2</sub>, CH and C), S denotes the stoichiometric surface, V<sub>O</sub>(n) = defective surface with a V<sub>O</sub>(n) ( $n = 1, 2$ ) oxygen vacancy, and y is an index used for identifying specific adsorption configurations. y consists of a letter from “A” to “D”, where A denotes the surface iron atop site (on top of the Fe site on the surface layer), B denotes the surface oxygen atop site (on top of the O site on the surface layer), C denotes the Fe–O bridge site (between Fe and O on the surface layer) as shown in Fig. 3, D denotes the oxygen vacancy site, respectively. For example, CH@S-A corresponds to CH radicals ( $x = 1$ ) adsorbed at the Fe atop site ( $y = A$ ) on the stoichiometric surface; CH<sub>2</sub>@V<sub>O</sub>(1)-D is CH<sub>2</sub> ( $x = 2$ ) adsorbed at the oxygen vacancy site ( $y = D$ ) on the reduced surface with a V<sub>O</sub>(1) vacancy.

#### 3.2.1 Adsorption on a stoichiometric $\alpha$ -Fe<sub>2</sub>O<sub>3</sub>(001) surface.

We start by investigating the adsorption of CH<sub>4</sub> on the stoichiometric  $\alpha$ -Fe<sub>2</sub>O<sub>3</sub>(001) surface so that we can obtain energy and structural information for the comparison of adsorption with vacancies. Various adsorption configurations on the stoichiometric  $\alpha$ -Fe<sub>2</sub>O<sub>3</sub>(001) surface are modeled, optimized and calculated as reported in Table 2. For the considered configurations, the methane molecule shows weak interaction with the  $\alpha$ -Fe<sub>2</sub>O<sub>3</sub>(001) surface. In the most favorable case, CH<sub>4</sub> adsorbs at the iron site as shown in Fig. 3(right), with an adsorption energy of 5.78 kJ mol<sup>−1</sup>. The distance between the C atom and the Fe site in this case is 2.98 Å.

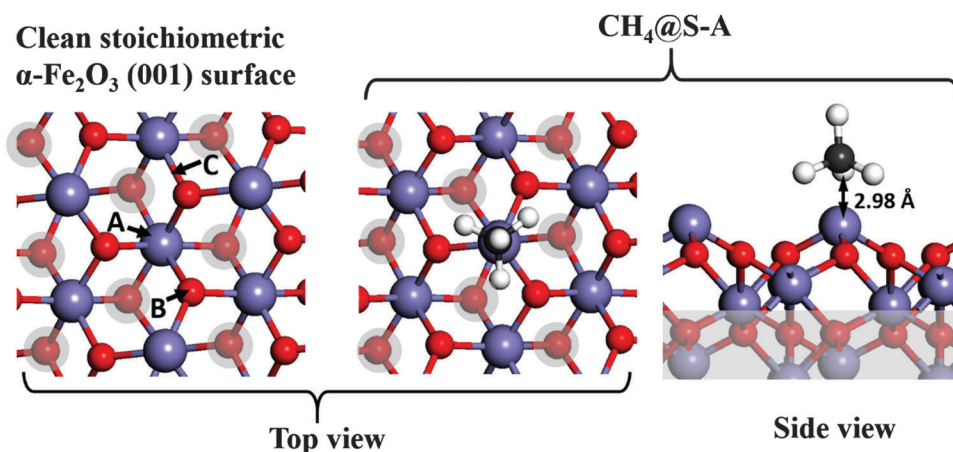


**Fig. 3** Adsorption sites on the stoichiometric  $\alpha$ -Fe<sub>2</sub>O<sub>3</sub>(001) surface and the most stable CH<sub>4</sub> adsorption configuration CH<sub>4</sub>@S-A. The red ball with a gray circle in the top view and a gray area in the side view represent the oxygen atom on the subsurface and the subsurface layer, respectively. The distance between the C atom and the closest surface Fe atom is indicated.



The O atop and Fe–O bridge adsorptions show lower stability with an adsorption energy of  $2.81 \text{ kJ mol}^{-1}$  and  $3.02 \text{ kJ mol}^{-1}$ , respectively. All these energy values are very small, showing a weak interaction between  $\text{CH}_4$  and the stoichiometric  $\alpha\text{-Fe}_2\text{O}_3(001)$  surface.

In order to obtain insights into the analysis of  $\text{CH}_4$  dissociation on the  $\alpha\text{-Fe}_2\text{O}_3(001)$  surface, we examine the adsorption of  $\text{CH}_x$  radicals.  $\text{CH}_3$  is the first intermediate during  $\text{CH}_4$  dissociation, and two stable adsorption configurations are found. In the most stable configuration,  $\text{CH}_3\text{@S-A}$ , the C atom in  $\text{CH}_3$  is directly bonded to the surface iron site. In this case, the charge is transferred from the surface to the adsorbed  $\text{CH}_3$ . This configuration has an adsorption energy of  $31.57 \text{ kJ mol}^{-1}$ . In the second stable configuration,  $\text{CH}_3\text{@S-C}$ ,  $\text{CH}_3$  is bonded to the Fe–O bridge site with the Fe–C bond of  $2.75 \text{ \AA}$  and the C–O bond of  $1.89 \text{ \AA}$ .  $\text{CH}_3\text{@S-C}$  is found to be  $7.86 \text{ kJ mol}^{-1}$  less stable than  $\text{CH}_3\text{@S-A}$ . The formed C–O bond shows single bond character (C–O bond order  $n = 0.97 \approx 1$ ). We also performed calculations on the adsorption of  $\text{CH}_3$  at the oxygen atop site, but this led to spontaneous desorption of  $\text{CH}_3$  radicals.

For the adsorption of the  $\text{CH}_2$  radical on the  $\alpha\text{-Fe}_2\text{O}_3(001)$  surface, three stable adsorption configurations are found.  $\text{CH}_2$  adsorption at the iron atop site  $\text{CH}_2\text{@S-A}$  is the most stable  $\text{CH}_2$  adsorption configuration with an adsorption energy of  $121.33 \text{ kJ mol}^{-1}$ . The second stable adsorption is  $\text{CH}_2$  adsorption at the oxygen atop site  $\text{CH}_2\text{@S-B}$ , which shows the adsorption energy of  $118.75 \text{ kJ mol}^{-1}$ . The third stable configuration  $\text{CH}_2\text{@S-C}$  is about  $30 \text{ kJ mol}^{-1}$  less stable than  $\text{CH}_2\text{@S-A}$ . For the CH radical, three different adsorption configurations are found.  $\text{CH}\text{@S-A}$  is the most stable configuration with  $273.67 \text{ kJ mol}^{-1}$  adsorption energy. The difference with the second stable configuration  $\text{CH}\text{@S-C}$  is small: the adsorption energy is only  $10.89 \text{ kJ mol}^{-1}$  higher for  $\text{CH}\text{@S-A}$  relative to  $\text{CH}\text{@S-C}$ . The oxygen atop site adsorption is relatively unstable with an adsorption energy of  $183.23 \text{ kJ mol}^{-1}$ . For a C radical adsorbed on the stoichiometric  $\alpha\text{-Fe}_2\text{O}_3(001)$  surface, we find three different stable adsorption configurations, which in order of stability are indicated as  $\text{CH}\text{@S-B}$ ,  $\text{CH}\text{@S-A}$  and  $\text{CH}\text{@S-C}$ .  $\text{CH}\text{@S-B}$  corresponds to the adsorption of C at the surface three-fold oxygen site O3c. Their adsorption energies are  $533.98$ ,  $467.26$  and  $435.38 \text{ kJ mol}^{-1}$ , respectively. The decrease in stability coincides with an increase in the Fe–C and C–O bond lengths, from  $1.98$  to  $2.38 \text{ \AA}$  and  $1.23$  to  $1.46 \text{ \AA}$ , respectively.

**3.2.2 Adsorption on the defective  $\alpha\text{-Fe}_2\text{O}_3(001)$  surface with oxygen vacancies.** Understanding the effect of oxygen vacancies on the adsorption of species on the surface is essential for a more fundamental understanding of lattice oxygen vacancy

migration in oxygen carriers and their reaction activity. Here, we therefore study the influence of the two most stable vacancies  $\text{V}_{\text{O}}(1)$  and  $\text{V}_{\text{O}}(2)$  on the adsorption of  $\text{CH}_4$  and  $\text{CH}_x$  radicals. We use D to denote the  $\text{V}_{\text{O}}(1)$  vacancy site when the oxygen vacancies are on the top surface, and also denote the  $\text{V}_{\text{O}}(2)$  vacancy if the oxygen vacancies are on the subsurface.

*i.  $\alpha\text{-Fe}_2\text{O}_3(001)$  surface with  $\text{V}_{\text{O}}(1)$  vacancy.* First, we study  $\text{CH}_4$  adsorption on the defective  $\alpha\text{-Fe}_2\text{O}_3(001)$  surface. We found that the interaction becomes repulsive when  $\text{V}_{\text{O}}(1)$  vacancy is created.  $\text{CH}_4$  still prefers to adsorb at the Fe atop site, but the neighboring oxygen vacancies make the adsorption energy of  $2.87 \text{ kJ mol}^{-1}$  lower than the adsorption energy on the stoichiometric surface  $\text{CH}_4\text{@S-A}$ .

For adsorption of  $\text{CH}_3$ , we previously found two stable adsorption configurations for the  $\text{CH}_3$  radical on the stoichiometric surface. However, four stable adsorption configurations are found on the reduced  $\alpha\text{-Fe}_2\text{O}_3(001)$  surface with  $\text{V}_{\text{O}}(1)$  vacancy. The strongest adsorption is the  $\text{CH}_3$  radical binding at the oxygen vacancy site to form  $\text{CH}_3\text{@V}_{\text{O}}(1)\text{-D}$  species with an adsorption energy of  $202.65 \text{ kJ mol}^{-1}$ , as shown in Fig. 4(a). The second and third stable configurations are  $\text{CH}_3$  adsorption at the Fe atop site  $\text{CH}_3\text{@V}_{\text{O}}(1)\text{-A}$  and  $\text{CH}_3$  adsorption at the Fe–O bridge site  $\text{CH}_3\text{@V}_{\text{O}}(1)\text{-C}$ . The adsorption energies for these two configurations are  $154.43$  and  $133.12 \text{ kJ mol}^{-1}$ . We can see that the adsorption strength on the surface with  $\text{V}_{\text{O}}(1)$  oxygen vacancy is higher than that on the stoichiometric surface. The presence of a  $\text{V}_{\text{O}}(1)$  vacancy thus stabilizes the adsorption of  $\text{CH}_3$  on a Fe atom and Fe–O bridge site in the proximity of this vacancy. In addition, O atop adsorption configuration  $\text{CH}_3\text{@V}_{\text{O}}(1)\text{-B}$  is found to be stable on the reduced surface with an adsorption energy of  $124.51 \text{ kJ mol}^{-1}$ , which is unfavorable for  $\text{CH}_3$  adsorption on the stoichiometric surface.

For adsorption of  $\text{CH}_2$ , the adsorption interactions of  $\text{CH}_2\text{@V}_{\text{O}}(1)\text{-A}$  and  $\text{CH}_2\text{@V}_{\text{O}}(1)\text{-D}$  are found to be nearly identical with an adsorption energy of  $317.42$  and  $309.14 \text{ kJ mol}^{-1}$ , respectively. Their adsorption configurations with bond length are shown in Fig. 4(b) and (c). The difference between the most stable adsorption of  $\text{CH}_2$  on the stoichiometric surface and the adsorption of  $\text{CH}_2$  on the reduced surface with a  $\text{V}_{\text{O}}(1)$  vacancy is  $196.09 \text{ kJ mol}^{-1}$ . Again, the influence of  $\text{V}_{\text{O}}(1)$  on the  $\text{CH}_2$  radical adsorption is similar for  $\text{CH}_3$  radicals. The adsorption strength at both Fe atop and O atop sites shows a great increase with the presence of a  $\text{V}_{\text{O}}(1)$  vacancy. However, Fe–O bridge site adsorption becomes unstable for  $\text{CH}_2$  radicals. The charge distribution with  $\text{V}_{\text{O}}(1)$  vacancy formation may cause the  $\text{CH}_2$  radical at the Fe–O bridge site to move toward the Fe atop site or the O atop site.

For the adsorption of CH on the stoichiometric surface two stable adsorption configurations were previously found as shown in Fig. 4(d) and (e). Also, in this case, the adsorption interaction was found to be almost identical for  $\text{CH}\text{@S-A}$  and  $\text{CH}\text{@S-C}$ . However, this does not lead to the same result when a  $\text{V}_{\text{O}}(1)$  vacancy is created. Similar to  $\text{CH}_2$  adsorption, the formation of vacancies makes Fe–O bridge adsorption unfavorable. However, the new adsorption configuration at the vacancy site

**Table 2** Adsorption energies (in  $\text{kJ mol}^{-1}$ ) of  $\text{CH}_4$  and  $\text{CH}_x$  radicals on the stoichiometric  $\alpha\text{-Fe}_2\text{O}_3(001)$  surface in different configurations

	$\text{CH}_x$ radicals				
	$\text{CH}_4$	$\text{CH}_3$	$\text{CH}_2$	CH	C
A. Fe atop	5.78	31.57	121.33	273.67	467.26
B. O atop	2.81	—	113.75	183.23	513.38
C. Fe–O bridge	3.02	23.71	90.24	262.78	435.38

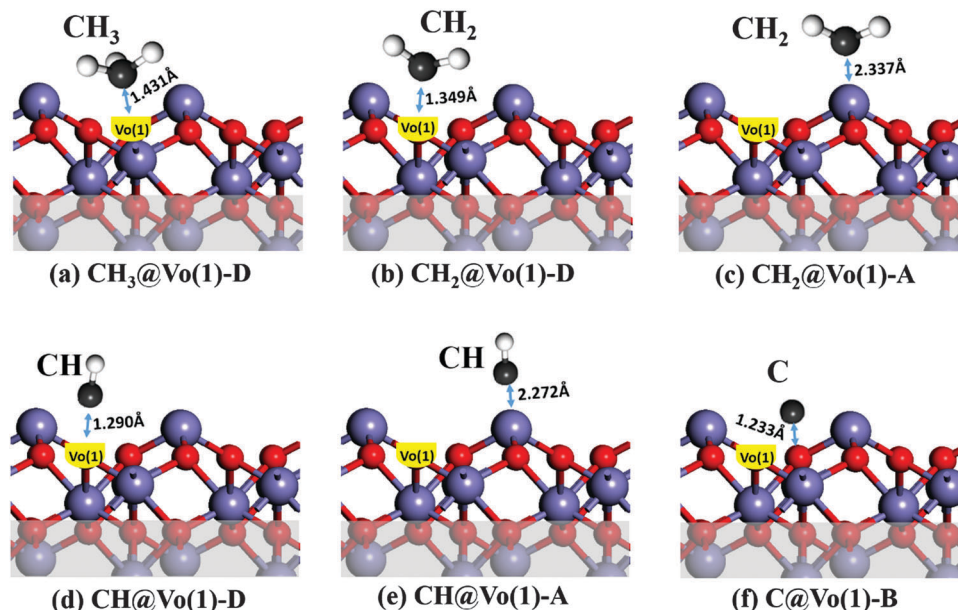


Fig. 4 The most stable  $\text{CH}_x$  radical adsorption configuration on the reduced  $\alpha\text{-Fe}_2\text{O}_3(001)$  surface with  $\text{V}_{\text{O}}(1)$  vacancy. The distance between the C atom and the closest surface atom is indicated.

$\text{CH@Vo}(1)\text{-D}$  shows approximately the same adsorption energy for CH ( $309.14 \text{ kJ mol}^{-1}$ ) as the adsorption of CH at the Fe atop site configuration  $\text{CH@Vo}(1)\text{-A}$  ( $317.42 \text{ kJ mol}^{-1}$ ).

Meanwhile, the Fe atop adsorption  $\text{CH@Vo}(1)\text{-A}$  becomes stronger than CH adsorption at the Fe atop site on the stoichiometric surface with  $117.29 \text{ kJ mol}^{-1}$  higher adsorption energy. For the C-radical adsorption, we find four different stable adsorption configurations on the reduced surface with  $\text{V}_{\text{O}}(1)$  vacancy, which in order of stability are indicated as  $\text{CH@Vo}(1)\text{-B}$ ,  $\text{CH@Vo}(1)\text{-A}$ ,  $\text{CH@Vo}(1)\text{-D}$  and  $\text{CH@Vo}(1)\text{-C}$ . The corresponding adsorption energies are  $489.62$ ,  $427.31$ ,  $410.65$  and  $392.83 \text{ kJ mol}^{-1}$ . The strongest adsorption form a C–O bond of  $1.223 \text{ \AA}$  as shown in Fig. 4(f). Compared with C radical adsorption on the stoichiometric surface, we found that the interaction between C and  $\alpha\text{-Fe}_2\text{O}_3(001)$  becomes weaker when the  $\text{V}_{\text{O}}(1)$  vacancy exists at neighboring adsorption sites. By this detailed study of the effect of a  $\text{V}_{\text{O}}(1)$  vacancy on  $\text{CH}_4$  and  $\text{CH}_x$  radical adsorption, we found that for  $\text{CH}_3$ ,  $\text{CH}_2$  and CH radicals the interaction energy increases relative to the most stable adsorption on the stoichiometric surface. However, for  $\text{CH}_4$  and C radicals, the adsorption energy dropped compared to the configurations on the stoichiometric surface. These results reveal the role of the  $\text{V}_{\text{O}}(1)$  vacancy in  $\text{CH}_4$  and  $\text{CH}_x$  radical adsorption on the iron oxide surface which can provide fundamental insight into the  $\text{CH}_x$  radical evolution mechanism with the formation of lattice oxygen vacancies on the top surface.

*ii.  $\alpha\text{-Fe}_2\text{O}_3(001)$  surface with  $\text{V}_{\text{O}}(2)$  vacancy.* Cheng *et al.* reported that the subsurface oxygen vacancies on the anatase  $\text{TiO}_2$  surface are more stable than oxygen vacancies on the top surface.<sup>32</sup> However, for the  $\alpha\text{-Fe}_2\text{O}_3(001)$  surface, we have shown that the subsurface oxygen vacancy  $\text{V}_{\text{O}}(2)$  is less stable than the top surface oxygen vacancy  $\text{V}_{\text{O}}(1)$ . At  $900^\circ\text{C}$ , the relative probability of  $\text{V}_{\text{O}}(2)$  is  $3.07\%$  thus its role in methane oxidation cannot be ignored.

For  $\text{CH}_4$  adsorption on the defective  $\alpha\text{-Fe}_2\text{O}_3(001)$  surface with  $\text{V}_{\text{O}}(2)$  vacancy, we found that the adsorption energy increases by  $1.22 \text{ kJ mol}^{-1}$  compared to the adsorption on the  $\alpha\text{-Fe}_2\text{O}_3(001)$  surface with  $\text{V}_{\text{O}}(1)$  vacancy and decreases by  $1.65 \text{ kJ mol}^{-1}$  compared to the stoichiometric surface though the Fe atop site is still the most favorable site. In the presence of  $\text{V}_{\text{O}}(2)$  vacancy, the Fe atop site again becomes the most favorable site for  $\text{CH}_3$  radicals and the adsorption energy is  $36.59 \text{ kJ mol}^{-1}$  higher than the adsorption energy at the  $\text{V}_{\text{O}}(2)$  oxygen vacancy site. Apart from the adsorption configurations  $\text{CH}_3@\text{V}_{\text{O}}(2)\text{-A}$ ,  $\text{CH}_3@\text{V}_{\text{O}}(2)\text{-C}$  and  $\text{CH}_3@\text{V}_{\text{O}}(2)\text{-D}$ , which have similar adsorption structure and orientation to the corresponding adsorption on the  $\alpha\text{-Fe}_2\text{O}_3(001)$  surface with  $\text{V}_{\text{O}}(1)$  vacancy, O atop configuration  $\text{CH}_3@\text{V}_{\text{O}}(2)\text{-B}$  is found to be unstable with a low adsorption energy ( $15.36 \text{ kJ mol}^{-1}$ ). This was close to the case for adsorption at the O atop site on the stoichiometric surface, where spontaneous desorption of  $\text{CH}_3$  occurs. Also, from Tables 3 and 4 we can see that a  $\text{V}_{\text{O}}(2)$  vacancy has a negative influence on the  $\text{CH}_3$  adsorption strength compared to a  $\text{V}_{\text{O}}(1)$  vacancy. Therefore, the migration of the  $\text{V}_{\text{O}}(2)$  oxygen vacancy to a  $\text{V}_{\text{O}}(1)$  vacancy can stabilize the adsorption of  $\text{CH}_3$  radicals on the iron oxide surface.

For adsorption of  $\text{CH}_2$ , it is found that the influence of the  $\text{V}_{\text{O}}(2)$  vacancy on  $\text{CH}_2@\text{V}_{\text{O}}(2)\text{-A}$  and  $\text{CH}_3@\text{V}_{\text{O}}(2)\text{-D}$  is almost identical, with an adsorption energy of  $236.58$  and  $251.47 \text{ kJ mol}^{-1}$ , respectively. The increase in the adsorption energy ranges from  $\sim 70 \text{ kJ mol}^{-1}$  for  $\text{CH}_2@\text{V}_{\text{O}}(2)\text{-C}$  to  $\sim 115 \text{ kJ mol}^{-1}$  for  $\text{CH}_2@\text{V}_{\text{O}}(2)\text{-A}$  relative to the adsorption on the stoichiometric surface. Compared to the stable  $\text{CH}_3$  adsorption on the  $\alpha\text{-Fe}_2\text{O}_3(001)$  surface with  $\text{V}_{\text{O}}(1)$  vacancy,  $\text{V}_{\text{O}}(2)$  vacancy results in a drop in the adsorption strength, and the highest adsorption energy ( $\text{CH}_3@\text{V}_{\text{O}}(2)\text{-D}$ ) drops by  $57.67 \text{ kJ mol}^{-1}$ . In this case, the Fe–C–Fe angle is  $78.8^\circ$ , compared to  $62.7^\circ$  for  $\text{CH}_3@\text{V}_{\text{O}}(1)\text{-D}$ ,

**Table 3** Adsorption energies (in  $\text{kJ mol}^{-1}$ ) of  $\text{CH}_4$  and  $\text{CH}_x$  radicals on the reduced  $\alpha\text{-Fe}_2\text{O}_3(001)$  surface with  $\text{V}_{\text{O}}(1)$  vacancy

	$\text{CH}_x$ radicals				
	$\text{CH}_4$	$\text{CH}_3$	$\text{CH}_2$	$\text{CH}$	$\text{C}$
A. Fe atop	2.91	154.43	317.42	390.96	427.31
B. O atop	1.76	124.51	267.26	276.91	489.62
C. Fe–O bridge	1.88	133.12	173.28	193.85	392.83
D. Vacancy	—	202.65	309.14	384.49	410.65

**Table 4** Adsorption energies (in  $\text{kJ mol}^{-1}$ ) of  $\text{CH}_4$  and  $\text{CH}_x$  radicals on the defective  $\alpha\text{-Fe}_2\text{O}_3(001)$  surface with  $\text{V}_{\text{O}}(2)$  vacancy

	$\text{CH}_x$ radicals				
	$\text{CH}_4$	$\text{CH}_3$	$\text{CH}_2$	$\text{CH}$	$\text{C}$
A. Fe atop	4.13	135.82	236.58	353.82	476.59
B. O atop	3.77	15.36	186.21	213.51	527.33
C. Fe–O bridge	2.10	129.23	166.29	272.32	469.27
D. Vacancy	2.13	89.11	251.47	344.22	489.61

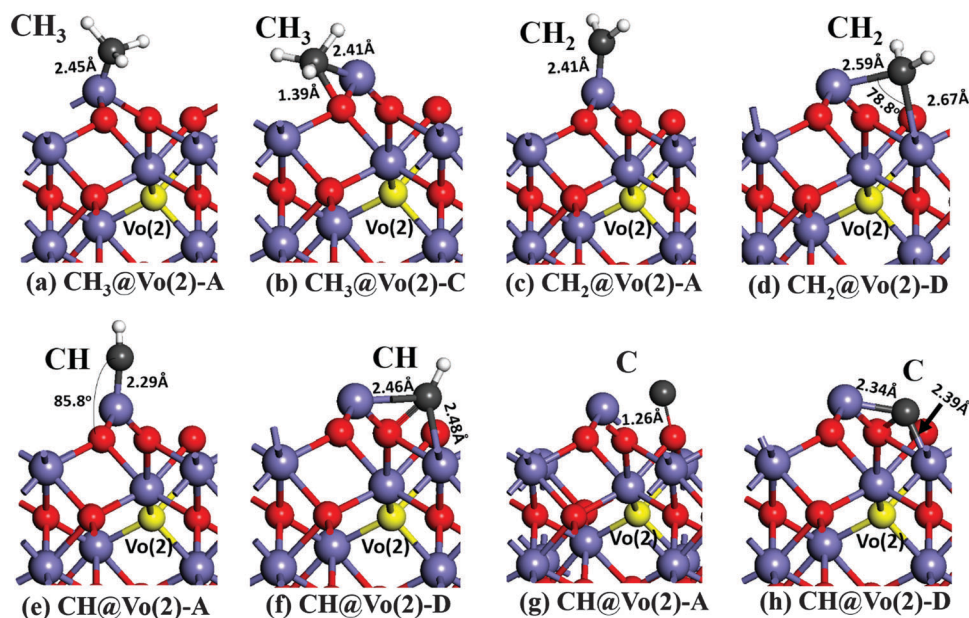
and the two Fe–C bonds are elongated from 2.23 and 2.39 Å to 2.59 and 2.67 Å, respectively.

CH adsorption is found to be enhanced when  $\text{V}_{\text{O}}(2)$  is located below the C of the adsorbent, and the strength of adsorption is decreased when  $\text{V}_{\text{O}}(2)$  is located on the side of the O3c of the Fe–C–O–Fe structure. The presence of  $\text{V}_{\text{O}}(2)$  leads to a shortening of the Fe–C bond in Fe atop adsorption configuration from 2.38 Å on the stoichiometric surface to 2.29 Å. The adsorption interactions of  $\text{CH@Vo}(2)\text{-A}$  and  $\text{CH@Vo}(2)\text{-D}$  are also nearly identical with an adsorption energy of 353.82 and 344.22  $\text{kJ mol}^{-1}$ , respectively. Their adsorption configurations with the bond length are shown in Fig. 5(e) and (f). The difference between the most stable adsorption of CH radicals on the stoichiometric surface and

the adsorption of CH on the defective surface with a  $\text{V}_{\text{O}}(2)$  vacancy is  $\sim 80 \text{ kJ mol}^{-1}$ . The adsorption energy for O atop configuration  $\text{CH@Vo}(2)\text{-B}$  drops by 63.4  $\text{kJ mol}^{-1}$  relative to  $\text{CH@Vo}(1)\text{-B}$ . While CH is adsorbed at the Fe–O bridge site in the  $\text{CH@Vo}(2)\text{-C}$  configuration, it is bonded to two O3c and the two Fe above the removed oxygen. It folds inward in the direction of the  $\text{V}_{\text{O}}(2)$  vacancy, with a Fe–C–O angle of  $65.3^\circ$ . In this configuration, the O3c–C bond lengths are decreased from 1.42 Å (C–O bond order  $n = 1$ ) in  $\text{CH@S-C}$  to 1.37 Å (C–O bond order  $n = 1.22$ ). The Fe–O site adsorption energy also increases slightly relative to  $\text{CH@S-C}$  ( $\Delta E_{\text{ad}} \approx 10 \text{ kJ mol}^{-1}$ ).  $\text{CH@Vo}(2)\text{-C}$  on the other hand leads to surface relaxation, which causes the neighboring Fe–O bonds to elongate to  $\sim 2.15$  Å.

For the adsorption of C radicals, the adsorption at the O atop site  $\text{C@Vo}(2)\text{-B}$  shows the highest adsorption energies (527.33  $\text{kJ mol}^{-1}$ ) while other three stable configurations:  $\text{C@Vo}(2)\text{-A}$ ,  $\text{C@Vo}(2)\text{-C}$  and  $\text{C@Vo}(2)\text{-D}$ , give an adsorption energy of 476.59  $\text{kJ mol}^{-1}$ , 469.27  $\text{kJ mol}^{-1}$  and 489.61  $\text{kJ mol}^{-1}$ , respectively. Compared to the adsorption on the stoichiometric surface, we can find that the subsurface oxygen vacancy slightly facilitates the C radical adsorption.

iii.  $\alpha\text{-Fe}_2\text{O}_3(001)$  surface with a  $\text{Vo}(1) + \text{Vo}(2)$  vacancy. We extend our study to the  $\alpha\text{-Fe}_2\text{O}_3(001)$  surface with a  $\text{Vo}(1)$  vacancy and a  $\text{Vo}(2)$  vacancy below the  $\text{Vo}(1)$  vacancy. Difference in the adsorption energy of the adsorption configurations on the defective  $\alpha\text{-Fe}_2\text{O}_3(001)$  surface, relative to the adsorption on the stoichiometric surface, is summarized and plotted in Fig. 6. In Fig. 6(A), we can see that the oxygen vacancy formation slightly decreases the interaction between  $\text{CH}_4$  and the iron oxide surface, also the interaction between C radicals and the iron oxide surface. For  $\text{CH}_3$  radicals adsorption at the Fe atop site, the  $\text{Vo}(1) + \text{Vo}(2)$  co-effect can increase the adsorption

**Fig. 5** The stable  $\text{CH}_x$  radicals adsorption configurations on the reduced  $\alpha\text{-Fe}_2\text{O}_3(001)$  surface with  $\text{V}_{\text{O}}(2)$  vacancy (yellow ball).



energy of  $152.21 \text{ kJ mol}^{-1}$  compared to no vacancies, which is 23.8% stronger than the effect of Vo(1) vacancy. For  $\text{CH}_2$  radicals, the adsorption with the Vo(1) + Vo(2) co-effect is only 2.1% stronger than the adsorption on the defective surface with one Vo(1) vacancy. However, the formation of the Vo(2) vacancy below the Vo(1) vacancy greatly increases the adsorption energy ( $\sim 200 \text{ kJ mol}^{-1}$ ) compared to adsorption on the stoichiometric surface. For CH radicals, the adsorption with the Vo(1) + Vo(2) co-effect is 8% stronger than the adsorption on the defective surface with one Vo(1) vacancy.

The difference between the adsorption energy of Fe–O bridge adsorption configurations of  $\text{CH}_x$  radicals on the  $\alpha\text{-Fe}_2\text{O}_3(001)$  surface with a Vo(1) vacancy and that with Vo(1) + Vo(2) vacancies is shown in Fig. 6(C). We can see, for Fe–O bridge site adsorption, that Vo(2) vacancy formation exhibits a negative effect on  $\text{CH}_3$ ,  $\text{CH}_2$  and CH radical adsorption. The adsorption strength is 26.2%, 9.2% and 4.7% lower than the strength on the surface with only the Vo(1) vacancy. This is because the co-effect of surface relaxation due to the surface oxygen removal and the Fe–C–O complex formation due to CH radical adsorption shortens the Fe–O bond, which causes elongation of the formed C–O bond. In addition, compared to Fe atop adsorption and O atop adsorption, the Vo(1) + Vo(2) co-effect has a relatively weak effect on the Fe–O bridge adsorption of  $\text{CH}_3$ ,  $\text{CH}_2$  and CH. In the presence of the Vo(1) and Vo(2) vacancy, the adsorption energy of  $\text{CH}_3$  binding at the Fe–O bridge site is  $80.69 \text{ kJ mol}^{-1}$  higher than that on the stoichiometric surface, while it is  $75.33 \text{ kJ mol}^{-1}$  higher for  $\text{CH}_2$  radicals and  $89.14 \text{ kJ mol}^{-1}$  higher for CH radicals. In contrast, the adsorption energy of  $\text{CH}_3$  binding at the O atop site of the surface with Vo(1) and Vo(2) vacancy is  $140.5 \text{ kJ mol}^{-1}$  higher than that on the stoichiometric surface, and it is  $157.75 \text{ kJ mol}^{-1}$  higher for  $\text{CH}_2$  radicals. We also can see from Fig. 6 that the formation of the subsurface oxygen vacancies can further stabilize the adsorption of  $\text{CH}_3$ ,  $\text{CH}_2$  and CH radicals at the Fe atop site or the O atop site.

To investigate the Van der Waals interaction effect on adsorption on the stoichiometric and defective surfaces, we also calculated the dispersion energies using Grimme's DFT-D2<sup>56</sup> and found that the inclusion of this correction results in an increase in the adsorption energy by about  $1\text{--}4 \text{ kJ mol}^{-1}$  eV for  $\text{CH}_x$  species adsorption. For example, the adsorption energy for  $\text{CH}_3$ @Vo(1)-D is  $202.65 \text{ kJ mol}^{-1}$  without dispersion while it is  $204.93 \text{ kJ mol}^{-1}$  with dispersion. Therefore, the Van der Waals interaction should not significantly affect the adsorption of  $\text{CH}_x$  species. This is because the adsorption of  $\text{CH}_x$  species is quite strong, and thus, dispersive forces play only a small role.

### 3.3 Effect of oxygen vacancies on the distribution of adsorbed $\text{CH}_4$ and $\text{CH}_x$ ( $x = 0\text{--}3$ ) radicals

We have shown that the presence of oxygen vacancies on the  $\alpha\text{-Fe}_2\text{O}_3(001)$  surface can significantly influence the adsorption of  $\text{CH}_4$  and  $\text{CH}_x$  ( $x = 0\text{--}3$ ) radicals. Here we further analyze the probability of finding an adsorbed species either in a stoichiometric region of the surface or at or near an oxygen vacancy under equilibrium conditions. We divided the surface into two

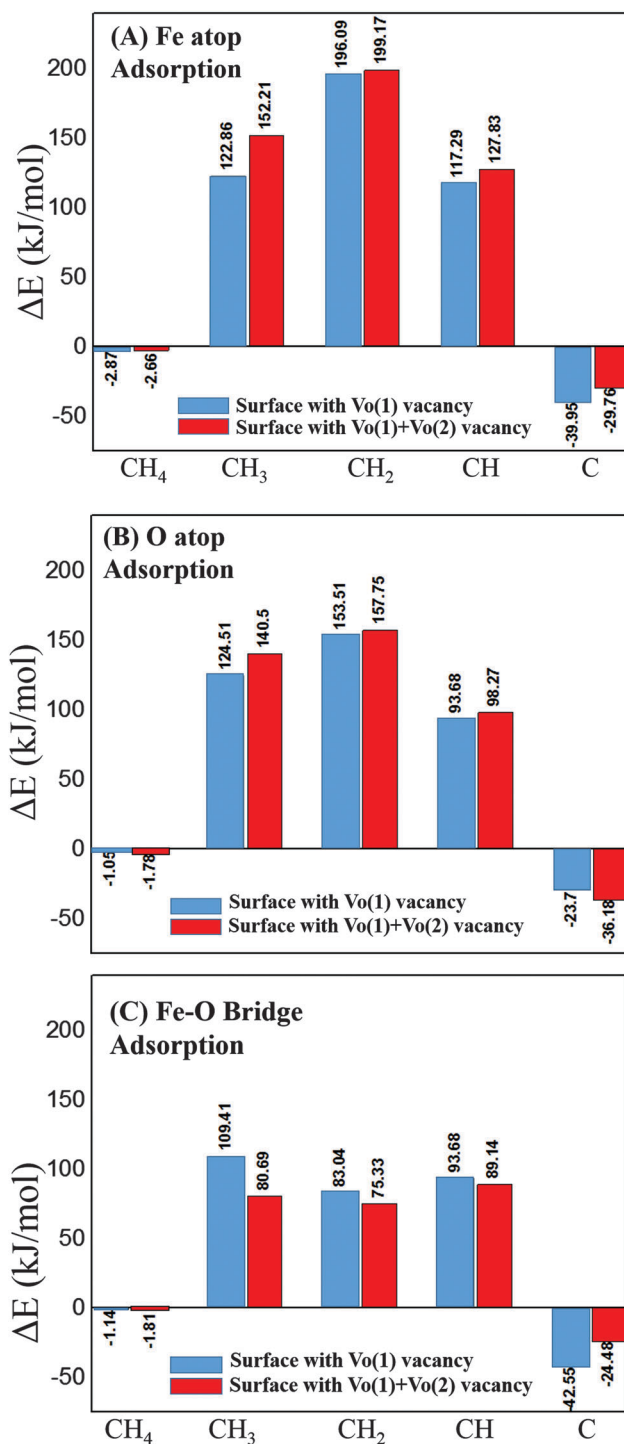


Fig. 6 Difference in the adsorption energy of the adsorption configurations of  $\text{CH}_4$  and  $\text{CH}_x$  radicals on the  $\alpha\text{-Fe}_2\text{O}_3(001)$  surface with Vo(1) vacancy (blue bar) or Vo(1) + Vo(2) vacancy (red bar) relative to the adsorption on the stoichiometric surface.

regions: a stoichiometric region, where no oxygen vacancies exist near the adsorbed species, one region with Vo(1) vacancy or Vo(1) + Vo(2) vacancy. We use  $s$  to denote the stoichiometric surface,  $d$  for the defective region with Vo(1) vacancy or Vo(1) + Vo(2) vacancy.



Firstly, at temperature  $T$ , the average lifetime  $\rho_i$  of the adsorbed species  $i$  in the most stable configuration  $j$  can be calculated using the Frenkel equation:<sup>57</sup>

$$\rho_{i,j} = \frac{1}{v_{i,j}} \times \exp\left(\frac{E_{\text{ad},i,j}}{k_B T}\right) \quad (4)$$

where  $v_{i,j}$  is the vibrational frequency of the adsorbed species  $i$  in the configuration  $j$ ,  $k_B$  is the Boltzmann constant and  $E_{\text{ad},i,j}$  is the adsorption energy of the species  $i$  in adsorption configuration  $j$ . Then we can obtain the probability of finding the adsorbed species  $i$  in configuration  $j$  in the defective region  $d$  using eqn (5):

$$P_i = \frac{\sum_j^d (n_{i,j} \times \rho_{i,j})}{\sum_j^s (n_{i,j} \times \rho_{i,j}) + \sum_j^d (n_{i,j} \times \rho_{i,j})} \quad (5)$$

where  $n_{i,j}$  is the percentage of adsorption sites for the species  $i$  adsorption with configuration  $j$ .  $\sum_j^s (n_{i,j} \times \rho_{i,j})$  which is the sum of the product of the average lifetime and the percentage of adsorption sites for the adsorbed species  $i$  with each stable configuration  $j$  in the stoichiometric region. The configuration  $j$  refers to Fe atop, O atop and Fe–O bridge adsorption configuration; thus the sum is taken over three different configurations. For the defective region, the configuration  $j$  also refers to vacancy adsorption configuration besides Fe atop, O atop and Fe–O bridge adsorption configuration, thus the sum  $\sum_j^d (n_{i,j} \times \rho_{i,j})$  is taken over four different configurations.

We give weights based on the vacancy equilibrium distribution on the defective surface at different temperatures. Obviously,  $\text{Vo}(1)$  has a greater influence on the adsorption distribution because of a much higher abundance on the surface compared to  $\text{Vo}(2)$ . Also,  $\text{Vo}(1)$  is easier to form than  $\text{Vo}(2)$  due to lower vacancy formation energy as shown in Table 1. When the first oxygen vacancy  $\text{Vo}(1)$  is created, the vacancy concentration in the  $s + d$  region is 0.33%. The second, third and fourth vacancies also appear at the top surface. The distance between neighboring  $\text{Vo}(1)$  vacancies is about 5 Å. The fifth vacancy will form on the subsurface of the  $d$  region and the  $\text{Vo}(2)$  vacancy formation energy is 39.5 kJ mol<sup>−1</sup> lower than that on the top surface. We have examined  $\text{CH}_4$  adsorption on the stoichiometric surface, the defective surface with a  $\text{Vo}(1)$  vacancy and with a  $\text{Vo}(2)$  vacancy, and found the most stable adsorption configurations with adsorption energies of 5.78 kJ mol<sup>−1</sup>, 2.91 kJ mol<sup>−1</sup> and 4.13 kJ mol<sup>−1</sup>, respectively. It cannot be accurate to calculate the probability of finding  $\text{CH}_4$  based on these small values due to the weak interaction with the surfaces. Therefore, we only investigate the probability of finding  $\text{CH}_x$  species. For  $\text{CH}_x$  radicals, at 900 °C, the calculated probability in the defective regions of the surface is shown in Fig. 7.

From Fig. 7, we can see the probability of finding the adsorbed  $\text{CH}_3$  radical in the defective region  $d$  dramatically increases when oxygen vacancies are formed. It is 73% for

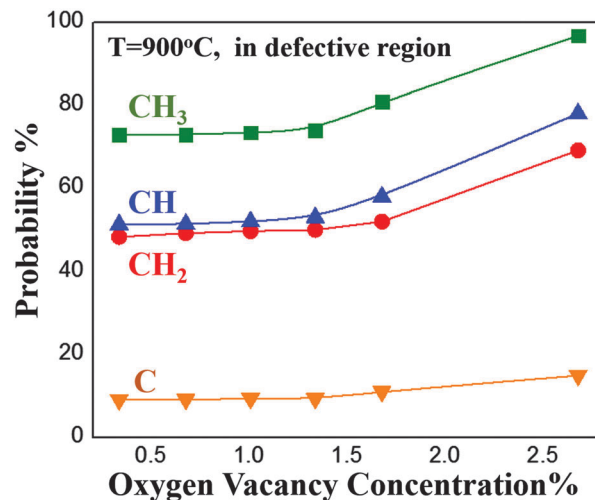


Fig. 7 Oxygen vacancy concentration dependence of the probability of finding an adsorbed  $\text{CH}_x$  radical in the defective region of the  $\alpha\text{-Fe}_2\text{O}_3(001)$  surface.

0.33% vacancy concentration. On the other hand, the probability of finding the adsorbed  $\text{CH}_3$  radical in the stoichiometric region  $s$  greatly increases upon this vacancy formation. However, when the oxygen vacancy concentration is between 0.33% and 1.33%, the  $\text{CH}_3$  radical probability in the defective region almost remains constant with the increase in the oxygen vacancy concentration. It is because the newly formed vacancy in the defective region has a very weak effect on the  $\text{CH}_3$  radical adsorption due to the distance of  $\sim 5$  Å. When the oxygen vacancy concentration further increases to 1.67%, which responds to the fifth oxygen vacancy formation on the subsurface, the  $\text{CH}_3$  radical probability in the defective region reaches 81.3%. For a vacancy concentration of higher than 2.5%, we found that the  $\text{CH}_3$  probability increases to 95%. This can be explained by the strong interaction between the  $\text{CH}_3$  radical and the oxygen vacancy site. Although the vacancy sites may not be enough for all  $\text{CH}_3$  adsorption to form  $\text{CH}_3\text{@Vo}(1)\text{-D}$  configuration when the vacancy concentration is only 2.67%, the probability of 96.7% illustrates that  $\text{CH}_3$  radicals prefer to be adsorbed onto Fe atop sites, O atop sites or Fe–O bridge sites which are close to vacancies, to form  $\text{CH}_3\text{@Vo}(1)\text{-A}$ ,  $\text{CH}_3\text{@Vo}(1)\text{-B}$  or  $\text{CH}_3\text{@Vo}(1)\text{-C}$  configurations, rather than  $\text{CH}_3\text{@S-A}$  or  $\text{CH}_3\text{@Vo}(1)\text{-C}$ .

For the  $\text{CH}_2$  radical, we found that the probability in the defective region is about 49.5% when the oxygen vacancy concentration is between 0.33 and 1.33%. It indicates that there is almost the same amount of adsorbed  $\text{CH}_2$  radicals in the stoichiometric region with the amount in the defective region when the vacancy concentration is very low. It agrees with the fact that  $\text{CH}_2$  radicals show the preferential adsorption towards both Fe site and the oxygen vacancy site with almost the same adsorption energies. Similarly, for  $\text{CH}$  radicals, we found that the probability in the defective region is about 51% when the oxygen vacancy concentration is in the same range. When the oxygen vacancy concentration increases to 2.67%, the probabilities of adsorbed  $\text{CH}_2$  and  $\text{CH}$  in the defective region increase up to 69.2% and 78.1%, respectively. In other words, when the vacancy concentration increases, the probability of

finding the adsorbed CH<sub>2</sub> and CH radicals in the stoichiometric region also decreases. However, from Fig. 7 we can see that there are still 30.8% CH<sub>2</sub> and 21.9% CH radicals in the stoichiometric region even when the vacancy concentration is higher than 2.5%. This means that a fraction of CH<sub>2</sub> and CH radicals obtained by CH<sub>3</sub> dissociation can migrate to the Fe atop site in the non-defective region from vacancy sites where most CH<sub>3</sub> radicals reside. Considering the adsorption stability, these adsorbed CH<sub>2</sub> radicals will prefer to be in CH<sub>2</sub>@S-A configuration in the stoichiometric region, and CH@Vo(1)-A and CH@Vo(1)-D configuration in the defective region. Likewise, we can conclude that the adsorbed CH radicals will prefer to be in CH@S-A configuration in the stoichiometric region, and CH@Vo(1)-A and CH@Vo(1)-D configuration in the defective region.

From Fig. 7 we can see that the probability of finding the adsorbed C in the defective region is relatively low, compared to other CH<sub>x</sub> radicals. It is about ~9% when the oxygen vacancy concentration is less than 2%. Different from the probability for CH<sub>3</sub>, CH<sub>2</sub> and CH radicals, the probability of finding the adsorbed C in the defective region will not significantly increase when the oxygen vacancy concentration is higher than 2.5%. It is only 14.3% when the oxygen vacancy is 2.67%. This can be explained by the fact that the formation of oxygen vacancy decreases the adsorption strength of C radicals. Thus, a large percentage of C radicals prefer to be adsorbed in the stoichiometric region, which can be called as C deposition leading to a decrease in the activity of the  $\alpha$ -Fe<sub>2</sub>O<sub>3</sub> surface.

The above-mentioned results clearly show that oxygen vacancies significantly influence the distribution of the adsorbed species at the surface and determine the adsorption configuration under equilibrium conditions. Increasing the oxygen vacancy concentration can cause higher probability of finding adsorbed CH<sub>x</sub> (0–3) radicals in the defective region. Because of the strong interaction between CH<sub>x</sub> radicals and oxygen vacancies, a higher oxygen vacancy concentration can lead to a stronger adsorption for CH<sub>3</sub>, CH<sub>2</sub> and CH, or a weaker adsorption of C radicals, hence facilitating the surface reactions or reducing the C deposition. In addition, the probability analysis reveals the relation between structures and the adsorption position, also the possible migration paths of CH<sub>x</sub> radicals on the surface. These results are essential for understanding of CH<sub>4</sub> reaction on iron oxides.

### 3.4 CH<sub>4</sub> dissociation on defective $\alpha$ -Fe<sub>2</sub>O<sub>3</sub> surfaces

We have investigated the adsorption of CH<sub>4</sub> and CH<sub>x</sub> radicals on stoichiometric and defective  $\alpha$ -Fe<sub>2</sub>O<sub>3</sub>(001) surfaces with oxygen vacancies. Based on the obtained adsorption configurations and adsorption energies, we can explore the CH<sub>4</sub> dissociation pathways and further reveal the role of oxygen vacancies of  $\alpha$ -Fe<sub>2</sub>O<sub>3</sub>(001) surfaces.

In the oxygen carrier reduction section of the chemical looping system, adsorbed CH<sub>4</sub> will sequentially dissociate into CH<sub>3</sub>, CH<sub>2</sub>, CH and C radicals, and the corresponding pathway can be mapped using the CI-NEB method. However, we need to correct the dissociation barriers using a thermochemistry

model because the reaction temperature in the chemical looping system is usually higher than 700 °C.

We previously developed a modified Brønsted–Evans–Polanyi relationship to calculate the activation energy for the elementary steps of the metathesis reaction.<sup>58</sup> Here, we extend this method to calculate the activation energy for CH<sub>4</sub> dissociation under chemical looping conditions as follows:

$$E_a(T) = E_{a,\text{DFT}} + \alpha(\Delta H_{\text{dis}}(T) - \Delta E_{\text{dis,DFT}}) \quad (6)$$

where  $E_{a,\text{DFT}}$  corresponds to the forward activation energy barrier at 0 K, which is obtained from CI-NEB calculations.  $\Delta H_{\text{dis}}(T)$  is the dissociation enthalpy at finite temperature, which is calculated from the individual enthalpies of the initial state and the final state for the constituent elementary reactions.  $\Delta E_{\text{dis,DFT}}$  is the difference between the energies of the final state and the initial state at 0 K. The variable  $\alpha$  denotes the relative position of the transition state compared to the initial (*i.e.*,  $\alpha = 0$ ) or final (*i.e.*,  $\alpha = 1$ ) state of the relevant elementary dissociation reaction. It can be obtained by considering which image in the CI-NEB calculations corresponds to the transition state. When the value of  $\alpha$  is close to 0, it describes an initial-like transition state; thus, the activation energy may be kept at the DFT value. When the value of  $\alpha$  is close to 1, it corresponds a final-like transition state and the activation energy is corrected using eqn (6).

To obtain enthalpy,  $H$ , estimates at finite temperature,  $T$ , for all adsorbed species and products, we correct the electronic energy for the zero point energy (ZPE) contribution and temperature variation using  $C_p$ :

$$H(T) = H(0 \text{ K}) + \int_0^T C_p(T') dT' \quad (7)$$

Numerically,  $T = 0 \text{ K}$  results in an undefined value during the evaluation of  $C_p$ , as the temperature appears in the denominator. We can approximate  $H(0 \text{ K}) \approx H(1 \text{ K})$ , and obtain its value by  $H(1 \text{ K}) = U(0 \text{ K}) + \text{ZPE}$ , where  $U$  is the total energy. The heat capacity  $C_p = T \left( \frac{\partial S}{\partial T} \right)_p$  can also be computed numerically by differentiating the entropy. The vibrational entropy,  $S_{\text{vib}}$ , can be directly obtained from the vibrational partition function using the DFT-calculated frequencies.

Because the H atom will be produced in CH<sub>4</sub> dissociation, we examined H adsorption and found that they have equal adsorption energies of about 263 kJ mol<sup>−1</sup> at the Fe atop site of the stoichiometric surface and the defective surface. However, for the oxygen atop site, the adsorption energies of H are 218 kJ mol<sup>−1</sup> on the stoichiometric surface, and 247 kJ mol<sup>−1</sup> on the defective surface, respectively. Based on the adsorption of CH<sub>4</sub> and the co-adsorption of CH<sub>3</sub> and H, the first step of CH<sub>4</sub> dissociation is examined and the reaction energy profile is mapped out, as shown in Fig. 8. T<sub>s</sub>1 denotes the transition state of CH<sub>4</sub> dissociation into CH<sub>3</sub> and H occurring on the stoichiometric surface while T<sub>d</sub>1 denotes the transition state of CH<sub>4</sub> dissociation which proceeds on the defective surface. On the stoichiometric  $\alpha$ -Fe<sub>2</sub>O<sub>3</sub>(001) surface, CH<sub>4</sub> dissociates on top of a Fe atom into CH<sub>3</sub> and H *via* the transition state T<sub>s</sub>1.

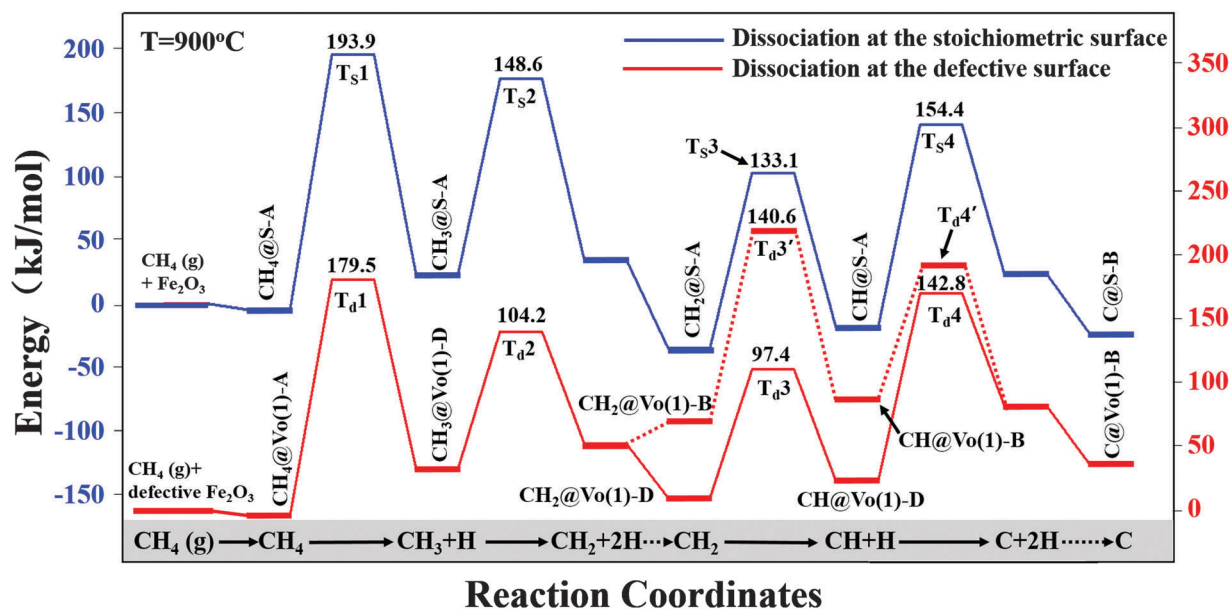


Fig. 8 Energy profile for CH<sub>4</sub> sequential dissociation on the stoichiometric and defective  $\alpha$ -Fe<sub>2</sub>O<sub>3</sub>(001) surface ( $T = 900^\circ\text{C}$ ). T<sub>S</sub> denotes the transition state on the stoichiometric  $\alpha$ -Fe<sub>2</sub>O<sub>3</sub>(001) surface and T<sub>d</sub> denotes the transition state on the defective surface.

The reaction needs to overcome the energy barrier of  $193.9\text{ kJ mol}^{-1}$ . In the transition state T<sub>S1</sub>, the breaking C–H bond is elongated to  $1.611\text{ \AA}$ , and the forming H–O bond is  $1.361\text{ \AA}$ . This reaction is endothermic by  $27.3\text{ kJ mol}^{-1}$ . On the defective  $\alpha$ -Fe<sub>2</sub>O<sub>3</sub>(001) surface, CH<sub>4</sub> dissociates *via* T<sub>d1</sub> along with CH<sub>3</sub> moving to the oxygen vacancy site while H remaining at the Fe atop site, and the corresponding barrier is  $14.4\text{ kJ mol}^{-1}$  lower than that on the stoichiometric surface.

Considering the most stable CH<sub>3</sub> adsorption configuration CH<sub>3</sub>@S-A on a stoichiometric surface as the initial state and co-adsorbed configuration of CH<sub>2</sub> and H as the final state, the transition state T<sub>S2</sub> of CH<sub>3</sub> dissociation is searched. We found that CH<sub>3</sub> dissociates into CH<sub>2</sub> and H along with H moving to another oxygen atop site which is opposite to the previous H obtained during the first step of CH<sub>4</sub> dissociation. The energy barrier is  $148.6\text{ kJ mol}^{-1}$ , and it is kinetically favorable compared with the first dissociation step. For the dissociation of CH<sub>3</sub> *via* T<sub>d2</sub> on the defective surface with Vo(1) vacancy, the calculated barrier is  $104.2\text{ kJ mol}^{-1}$ , which indicates that oxygen vacancies can greatly affect the second step of CH<sub>4</sub> dissociation. In the transition state T<sub>d2</sub>, the distance of the breaking C–H bond is stretched to  $1.685\text{ \AA}$ , and the forming bond length of H–Fe is shortened to  $1.396\text{ \AA}$ . This reaction is found to be endothermic by  $28.95\text{ kJ mol}^{-1}$ . On a defective surface with the top surface vacancy, the CH<sub>2</sub> radical shows preferential adsorption towards both the Fe atop site and the oxygen vacancy site, thus two reaction pathways are conceived for CH<sub>2</sub> dissociation on the  $\alpha$ -Fe<sub>2</sub>O<sub>3</sub>(001) surface with Vo(1) vacancy. In the transition state T<sub>d3</sub>, the breaking C–H bond is increased to  $1.741\text{ \AA}$ , and the forming H–Fe bond is shortened to  $1.372\text{ \AA}$ . This dissociation *via* T<sub>d3</sub> is also endothermic by  $12.54\text{ kJ mol}^{-1}$  and needs to overcome a barrier of  $97.4\text{ kJ mol}^{-1}$ . If the initial state is CH<sub>2</sub>@Vo(1)-B, the dissociation needs to overcome a barrier of  $140.6\text{ kJ mol}^{-1}$ ,

which is approximately equal to the barrier of CH<sub>2</sub> dissociation on the stoichiometric surface ( $133.1\text{ kJ mol}^{-1}$ ).

The last step of CH<sub>4</sub> full dissociation is the dehydrogenation of the methine radical CH to produce the C radical. We have found the C radical prefers to adsorb to O atop site both in the stoichiometric surface and the defective surface with oxygen vacancies. Co-adsorption of C and H atom has slight repulsive interaction compared with the sum of individual adsorption energies. On the stoichiometric surface, CH adsorption on Fe atop site is the most favorable configuration (CH@S-A). Based on these stable final states and initial states, we search for the local minimum on the potential energy surface and obtain a dissociation barrier of  $154.4\text{ kJ mol}^{-1}$  (T<sub>S4</sub>). In contrast, the most favorable configurations for CH on the defective surface with oxygen vacancies are CH@Vo(1)-A and CH@Vo(1)-D. Thus, we consider two possible reaction pathways for the dissociation of CH on the defective surface: (1) the H atom remains at the Fe atop site and the C atom diffuses from the Fe atop site to the O atop site; (2) the H atom binds to the neighboring O atop site and the C atom diffuses from the oxygen vacancy site to the O atop site. The calculated dissociation barriers for (1) and (2) pathways are  $146.33\text{ kJ mol}^{-1}$  and  $142.8\text{ kJ mol}^{-1}$  (T<sub>d4</sub>), respectively. If the initial state is CH@Vo(1)-B, the reaction barrier is even  $21.3\text{ kJ mol}^{-1}$  lower than the barrier of the second pathway where CH@Vo(1)-D is the initial state because no diffusion energy is required for this process. However, the O atop site is not favorable for CH adsorption, and the formation of CH@Vo(1)-B from CH<sub>2</sub>@Vo(1)-D must overcome a barrier of  $156.9\text{ kJ mol}^{-1}$  which is  $46.8\text{ kJ mol}^{-1}$  higher than the barrier of the most favorable CH<sub>2</sub> dissociation pathway, as shown as the red dashed line in Fig. 8. Therefore, the dissociation pathway *via* CH@Vo(1)-B configuration is unfavorable. To analyze the whole energy profile along the dissociation paths, we found the



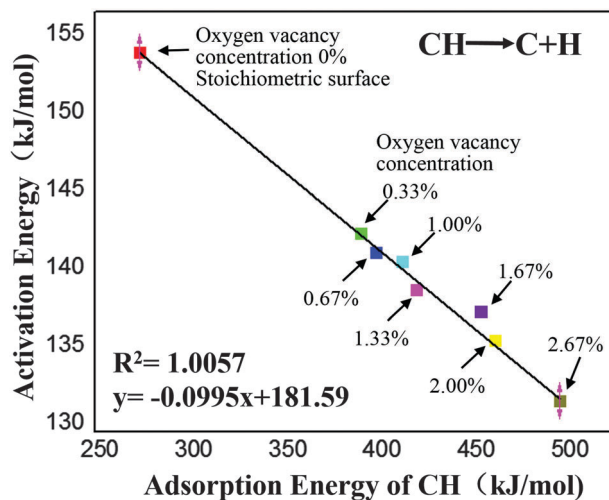


Fig. 9 Relationship between activation energy of the CH radical dissociation and adsorption energy of the CH radical. Oxygen vacancy concentration is labeled.

highest barrier is  $193.9 \text{ kJ mol}^{-1}$  for the dissociation on the stoichiometric surface, and  $179.5 \text{ kJ mol}^{-1}$  for the dissociation on the defective surface, respectively. They both are within the range of the reported experimental values ( $150\text{--}270 \text{ kJ mol}^{-1}$ ).<sup>59</sup>

Since we have found that oxygen vacancies can facilitate the CH radical adsorption, we can further analyze the vacancy effect on the CH dissociation. Fig. 9 presents a good ( $R^2 = 1.0057$ ) linear relationship between dissociation activation energy and the adsorption energy of the CH radical which is related to the vacancy position and concentration. We can see that the activation energy decreases with the increase of the adsorption energy of the CH radical on  $\alpha\text{-Fe}_2\text{O}_3(001)$  surfaces. In other words, weaker adsorption brings higher activation energy. It is in agreement with the fact that low adsorption energy of  $\text{CH}_x$  configurations is at high energy levels and thus they have to overcome a high activation energy barrier to dissociate. However, when the oxygen vacancy concentration is higher than 2.67%, increasing the oxygen vacancy concentration cannot continue to lower the CH dissociation barrier. Similar results are obtained for  $\text{CH}_3$  and  $\text{CH}_2$  dissociation. On the other hand, too high oxygen vacancy concentration will decrease the oxygen carrier capacity of donating lattice oxygen for partial oxidation of  $\text{CH}_4$ . Therefore, finding a suitable oxygen vacancy concentration is of great significance, which can lower the  $\text{CH}_4$  dissociation barriers meanwhile can provide enough lattice oxygen for  $\text{CH}_4$  partial oxidation. We have previously found that an inert support  $\text{TiO}_2$  can lower the vacancy formation energy thus can lead to the formation of oxygen vacancies.<sup>34</sup> Therefore, we can control the oxygen vacancy concentration of oxygen carriers to increase the activity of oxygen carriers by adding suitable support materials, which will be our future work.

## 4 Conclusion

*Ab initio* DFT+*U* calculations of methane and  $\text{CH}_x$  (0–3) radical adsorption on iron oxide was carried out to elucidate the geometries and energies of adsorption configurations on

stoichiometric and defective  $\alpha\text{-Fe}_2\text{O}_3(001)$  surfaces with oxygen vacancies. We found that top surface oxygen vacancies are the most stable vacancies, compared to oxygen vacancies on a subsurface and the next subsurface. In the presence of these vacancies, the adsorption strength of  $\text{CH}_4$  and C radicals on the  $\alpha\text{-Fe}_2\text{O}_3(001)$  surface decreases compared to that in the absence of vacancies, but it increases for methyl ( $\text{CH}_3$ ), methylene ( $\text{CH}_2$ ) and methine (CH) radicals. In contrast, the subsurface oxygen vacancy formation not only increases the adsorption strength of  $\text{CH}_3$ ,  $\text{CH}_2$  and CH radicals, but also facilitates C radical adsorption. However, oxygen vacancies on the subsurface have a smaller effect on  $\text{CH}_x$  radical adsorption compared to the top surface vacancies. The formation of the subsurface oxygen vacancies can stabilize the adsorption of  $\text{CH}_3$ ,  $\text{CH}_2$  and CH radicals. Specifically, the Fe atop site is the most favorable adsorption site for  $\text{CH}_4$  molecules. However, for the  $\text{CH}_3$  radical, the oxygen vacancy site is the most favorable adsorption site. The  $\text{CH}_2$  and CH radicals show preferential adsorption towards both the Fe atop site and the oxygen vacancy site, while the C radical prefers the O atop site on a defective surface.

The oxygen vacancies not only influence the adsorption strengths of  $\text{CH}_4$  and  $\text{CH}_x$  radicals on iron oxide, but also determine the distribution of  $\text{CH}_4$  and these corresponding radicals on the surface under equilibrium conditions. When the oxygen vacancy concentration is very low, increasing the oxygen vacancy concentration cannot cause higher probability of finding adsorbed  $\text{CH}_x$  radicals in the defective region. When the oxygen vacancy concentration is more than 2.5%, the probability of finding adsorbed  $\text{CH}_3$ ,  $\text{CH}_2$  and CH radicals in the defective region will evidently increase with the increase in the oxygen vacancy concentration. A higher oxygen vacancy concentration can lead to a stronger adsorption for  $\text{CH}_3$ ,  $\text{CH}_2$  and CH hence facilitating the surface reactions, or a weaker adsorption of C radicals, thus reducing C deposition. The probability analysis reveals the relation between structures and the adsorption position, also the possible migration paths of  $\text{CH}_x$  radicals on the surface.

In addition, oxygen vacancies can facilitate the  $\text{CH}_4$  dissociation on the iron oxide surface by lowering the dissociation barriers of  $\text{CH}_3$ ,  $\text{CH}_2$  and CH radicals. We found a linear relationship between the dissociation activation energy and the CH radical adsorption energy, which is determined by oxygen vacancy concentration. When the oxygen vacancy concentration is higher than 2.67%, increasing the oxygen vacancy concentration cannot continue to lower the CH dissociation barrier. Based on these results, future computational quantum mechanical and thermodynamic studies aiming to understanding methane partial oxidation can be envisaged. This study reveals the influence of oxygen vacancies on the  $\text{CH}_4$  and  $\text{CH}_x$  radical adsorption on iron oxide, and provides fundamental insights into the role of oxygen vacancies in the mechanism of  $\text{CH}_4$  dissociation for more active oxygen carrier design.

## Acknowledgements

The valuable support provided by the Supercomputer Center at The Ohio State University, and by the Texas Advanced Computing Cluster is gratefully acknowledged.

## References

- 1 L.-S. Fan, L. Zeng and S. Luo, *AIChE J.*, 2015, **61**, 2–22.
- 2 S. Bhavsar, M. Najera, R. Solunke and G. Vesper, *Catal. Today*, 2014, **228**, 96–105.
- 3 L.-S. Fan, L. Zeng, W. Wang and S. Luo, *Energy Environ. Sci.*, 2012, **5**, 7254–7280.
- 4 K. Li, H. Wang and Y. Wei, *J. Chem.*, 2013, 1–8.
- 5 A. Tong, D. Sridhar, Z. Sun, H. R. Kim, L. Zeng, F. Wang, D. Wang, M. V. Kathe, S. Luo, Z. Sun and L.-S. Fan, *Fuel*, 2013, **103**, 495–505.
- 6 F. He, Y. Wei, H. Li and H. Wang, *Energy Fuels*, 2009, **23**, 2095.
- 7 F. Li, R. Kim, D. Sridhar, F. Wang, L. Zeng, J. Chen and L.-S. Fan, *Energy Fuels*, 2009, **23**, 4182–4189.
- 8 L. F. de Diego, M. Ortiz, J. Adánez, F. García-Labiano, A. Abad and P. Gayán, *Chem. Eng. J.*, 2008, **144**, 289–298.
- 9 G. Azimi, T. Mattisson, H. Leion, M. Rydén and A. Lyngfelt, *Int. J. Greenhouse Gas Control*, 2015, **34**, 12–24.
- 10 T. Kodama, H. Ohtake, S. Matsumoto, A. Aoki, T. Shimizu and Y. Kitayama, *Energy*, 2000, **25**, 411–425.
- 11 A. Abad, F. García-Labiano, L. F. de Diego, P. Gayán and J. Adánez, *Energy Fuels*, 2007, **21**, 1843–1853.
- 12 J. Adánez, L. F. de Diego, F. García-Labiano, P. Gayán, A. Abad and J. M. Palacios, *Energy Fuels*, 2004, **18**, 371.
- 13 L.-S. Fan, *Chemical Looping Systems for Fossil Energy Conversions*, John Wiley & Sons, Hoboken, NJ, 2010.
- 14 T. Mattisson, A. Lyngfelt and P. Cho, *Fuel*, 2001, **80**, 1953–1962.
- 15 S. Luo, L. Zeng, D. Xu, M. Kathe, E. Chung, N. Deshpande, L. Qin, A. Majumder, T.-L. Hsieh, A. Tong, Z. Sun and L.-S. Fan, *Energy Environ. Sci.*, 2014, **7**, 4104–4117.
- 16 E. R. Monazam, R. W. Breault, R. Siriwardane, G. Richards and S. Carpenter, *Chem. Eng. J.*, 2013, **232**, 478–487.
- 17 Y. Jin, C. Sun and S. Su, *Phys. Chem. Chem. Phys.*, 2015, **17**, 16277.
- 18 D. R. Killelea, V. L. Campbell, N. S. Shuman and A. L. Utz, *Science*, 2008, **319**, 790–793.
- 19 R. R. Smith, D. R. Killelea, D. F. DelSesto and A. L. Utz, *Science*, 2004, **304**, 992.
- 20 B. L. Yoder, R. Bisson and R. D. Beck, *Science*, 2010, **329**, 553.
- 21 G. P. Krishnamohan, R. A. Olsen, G.-J. Kroes, F. Gatti and S. Woittequand, *J. Chem. Phys.*, 2010, **133**, 144308.
- 22 S. Nave and B. Jackson, *Phys. Rev. Lett.*, 2007, **98**, 173003.
- 23 A. K. Tiwari, S. Nave and B. Jackson, *Phys. Rev. Lett.*, 2009, **103**, 253201.
- 24 N. H. Linha, T. Q. Nguyen, W. A. Diñoa and H. Kasa, *Surf. Sci.*, 2015, **633**, 38–45.
- 25 Y. Pan, C. Liu, D. Mei and Q. Ge, *Langmuir*, 2010, **26**, 5551–5558.
- 26 Z. Cheng, B. J. Sherman and C. S. Lo, *J. Chem. Phys.*, 2013, **138**, 014702.
- 27 A. Kiejna, *Phys. Rev. B: Condens. Matter Mater. Phys.*, 2003, **68**, 235405.
- 28 D. Santos-Carballal, A. Roldan, R. Grau-Crespo and N. H. de Leeuw, *Phys. Chem. Chem. Phys.*, 2014, **16**, 21082–21097.
- 29 I. Goikoetxea, M. Alducin, R. Díez Muiñoab and J. I. Juaristiab, *Phys. Chem. Chem. Phys.*, 2012, **14**, 7471–7480.
- 30 R. M. Van Natter, J. S. Coleman and C. R. F. Lund, *J. Mol. Catal. A: Chem.*, 2008, **292**, 76–82.
- 31 Z. Cheng and C. S. Lo, *ACS Catal.*, 2012, **2**, 341–349.
- 32 H. Z. Cheng and A. Selloni, *Phys. Rev. B: Condens. Matter Mater. Phys.*, 2009, **79**, 092101.
- 33 O. Warschkow, D. E. Ellis, J. Hwang, N. Mansourian-Hadavi and T. O. Mason, *J. Am. Ceram. Soc.*, 2002, **85**, 213–220.
- 34 L. Qin, Z. Cheng, J. A. Fan, D. Kopechek, D. Xu, N. Deshpande and L.-S. Fan, *J. Mater. Chem. A*, 2015, **3**, 11302–11312.
- 35 P. Wanaguru, J. An and Q. Zhang, *Appl. Phys.*, 2016, **119**, 084302.
- 36 H. Ueta, L. Chen, R. D. Beck, I. Colón-Díaz and B. Jackson, *Phys. Chem. Chem. Phys.*, 2013, **15**, 20526–20535.
- 37 Z. Cheng and C. Lo, *Ind. Eng. Chem. Res.*, 2013, **52**, 15447–15454.
- 38 X. Shen, Z. Zhang and D. H. Zhang, *Phys. Chem. Chem. Phys.*, 2015, **17**, 25499–25504.
- 39 Z. Cheng, N. Fine and C. Lo, *Top. Catal.*, 2012, **55**, 345–352.
- 40 L. Wang, L. Wu, C. Dong, J. Zhang and W. Qin, *Appl. Mech. Mater.*, 2013, **345**, 298–301.
- 41 G. Kresse and J. Hafner, *Phys. Rev. B: Condens. Matter Mater. Phys.*, 1993, **47**, 558.
- 42 G. Kresse and J. Furthmüller, *Comput. Mater. Sci.*, 1996, **6**, 15.
- 43 G. Kresse and J. Furthmüller, *Phys. Rev. B: Condens. Matter Mater. Phys.*, 1996, **54**, 11169.
- 44 J. P. Perdew, K. Burke and M. Ernzerhof, *Phys. Rev. Lett.*, 1996, **77**, 3865.
- 45 P. E. Blöchl, *Phys. Rev. B: Condens. Matter Mater. Phys.*, 1994, **50**, 17953.
- 46 G. Kresse and D. Joubert, *Phys. Rev. B: Condens. Matter Mater. Phys.*, 1999, **59**, 1758.
- 47 P. E. Blöchl, O. Jepsen and O. K. Anderson, *Phys. Rev. B: Condens. Matter Mater. Phys.*, 1994, 16223.
- 48 R. L. Blake, R. E. Hessevic, T. Zoltai and L. W. Finger, *Am. Mineral.*, 1966, **51**, 123.
- 49 J. F. Herbst, R. E. Watson and J. W. Wilkins, *Phys. Rev. B: Solid State*, 1978, **17**, 3089.
- 50 V. I. Anisimov and O. Gunnarsson, *Phys. Rev. B: Condens. Matter Mater. Phys.*, 1991, **43**, 7570.
- 51 G. Rollmann, A. Rohrbach, P. Entel and J. Hafner, *Phys. Rev. B: Condens. Matter Mater. Phys.*, 2004, **69**, 165107.
- 52 W. Gordy, *J. Chem. Phys.*, 1947, **15**, 81.
- 53 D. Sheppard and G. Henkelman, *J. Comput. Chem.*, 2011, **32**, 1769–1771.
- 54 G. Henkelman, B. P. Uberuaga and H. J. Jonsson, *J. Chem. Phys.*, 2000, **113**, 9901.
- 55 Y. Wang, H. Sun, S. Tan, H. Feng, Z. Cheng, J. Zhao, A. Zhao, B. Wang, Y. Luo, J. Yang and J. G. Hou, *Nat. Commun.*, 2013, **4**, 2214.
- 56 S. Grimme, *J. Comput. Chem.*, 2006, **27**, 1787–1799.
- 57 J. Frenkel, *Z. Phys.*, 1924, **26**, 117–138.
- 58 Z. Cheng and C. S. Lo, *ACS Catal.*, 2015, **5**, 59–72.
- 59 D. Ghosh, A. K. Roy and A. Ghosh, *Trans. Iron Steel Inst. Jpn.*, 1986, **26**, 186–193.